Isogeometric Analysis of the electrophysiology in the human heart: numerical simulation of the bidomain equations on the atria

Luca Pegolotti[a,*], Luca Dedè[b], Alfio Quarteroni[b,c]

[a] *Institute of Mathematics, École Polytechnique Fédérale de Lausanne, Station 8, EPFL, CH–1015 Lausanne, Switzerland*
[b] *MOX—Modeling and Scientific Computing, Mathematics Department "F. Brioschi", Politecnico di Milano, via Bonardi 9, Milano, 20133, Italy*
[c] *Institute of Mathematics, École Polytechnique Fédérale de Lausanne, Station 8, EPFL, CH–1015 Lausanne, Switzerland (honorary professor)*

Abstract

We consider Isogeometric Analysis (IGA) for the numerical solution of the electrophysiology of the atria, which in this work is modeled by means of the bidomain equations on thin surfaces. First, we consider the bidomain equations coupled with the Roger-McCulloch ionic model on simple slabs. Here, our goal is to evaluate the effects of the spatial discretization by IGA and the use of different B-spline basis functions on the accuracy of the approximation, in particular regarding the accuracy of the front velocity and the dispersion error. Specifically, we consider basis functions with high polynomial degree, p, and global high order continuity, C^{p-1}, in the computational domain: our results show that the use of such basis functions is beneficial to the accurate approximation of the solution. Then, we consider a realistic application of the bidomain equations coupled with the Courtemanche-Ramirez-Nattel ionic model on the two human atria, which are represented by means of two NURBS surfaces.

Keywords: Isogeometric Analysis, cardiac electrophysiology, bidomain equations

1. Introduction

In the last few decades, the numerical simulation of the electric activity of the heart has become a valid tool for the study of the activation of the cardiac tissue [11, 55] both in physiological and pathological conditions. This process involves a wide range of scales, as well as several "characters" (physical variables) which interact in a complex fashion. Whole-heart models – i.e. models coupling the electrophysiology of heart with the mechanical response of the cardiac tissue [27, 37, 42] – provide meaningful information regarding ventricular arrhythmias and, specifically, the mechanisms underlying the self-sustained reentrant propagation of waves inside the myocardium [52]. Models of heart electrophysiology are typically based on several simplifying assumptions [40]: in particular, the cardiac muscle is often represented as a continuum, instead of an ensemble of myocites. For this reason, the properties of the cardiac cells and those of the tissue are encoded in microscopic and macroscopic models intrinsically coupled. While for the description of the microscopic behavior of the cells many models exist – we refer e.g. to [11] and [50] for a description of some of the most common ones – the bidomain model [28] is the standard choice for studying the propagation of the electric signal at the macroscopic scales of the tissue. Accurate approximations using the bidomain equations are however computationally expensive for various reasons [2]. As explained in [11], the steep propagating layer of the transmembrane potential – which has a thickness of about 0.5 mm – requires very thin meshes and small timesteps (1 ms or lower) in order to be accurately captured; moreover, the assumption of isolated material, i.e. of homogeneous Neumann boundary conditions imposed on the equations, often leads to ill-conditioned linear systems to be solved at each timestep. Because of these difficulties, the simpler monodomain model [10], which derives from the bidomain model under the assumption of equal anisotropic ratios in the intra- and extracellular spaces, is very often used to approximate

*Corresponding author
Email addresses: luca.pegolotti@epfl.ch (Luca Pegolotti), luca.dede@polimi.it (Luca Dedè), alfio.quarteroni@polimi.it (Alfio Quarteroni)

the electrophysiology of the heart. The monodomain model provides satisfactory results especially in physiological conditions [27], even if it lacks the detail and richness of the bidomain equations.

In this work, we focus on the solution of the bidomain equations on surfaces by using Isogeometric Analysis (IGA). IGA has already been used in [7, 8] for the solution of the bidomain model in three-dimensional cases and in [38] for solving the monodomain equations on the left atrium represented as a surface. In this paper, we solve the electrophysiology problem on the two atria by means of the bidomain equations coupled with suitable ionic models specifically tailored for atrial cells. We represent the atria as surfaces generated by NURBS basis functions. This approximation is motivated by the small thickness of the cardiac tissue in these chambers of the human heart: the same simplification has been adopted in [12] and [49]. In [49], surface representations of the atria have been considered together with three-dimensional ventricular geometries to reproduce the electrocardiogram by solving the bidomain equations with the Finite Element Method; the interaction of atria and vetricles was modeled by mimicking the role of the bundle of His and Purkinje fibers through a simplified model, i.e. using small values of the conductivity at the interface between the surfaces and the volumes. As explained in [49], the use of surfaces for the atria considerably reduces the computational cost of the bidomain equations while attaining a satisfactory accuracy of the model.

The advantages of IGA in this context are twofold. First, the computational domain is effectively identified with the physical domain in virtue of the isogeometric concept, which stands at the basis of IGA. In other words, the physical domain can be used without preprocessing (i.e. mesh generation) for the solution of the differential problem, so that the geometry is exactly preserved under h-refinement. Secondly, this method allows us to consider basis functions with high degree and high order of continuity, which is beneficial to the approximation of the steep front of the electric potential. Indeed, methods with highly regular basis functions – such as the spectral element method [5] and IGA [38] – have already been successfully employed for the solution of the monodomain equations; for example, in [38] it has been shown that IGA well captures the velocity of propagation of the front and manages to reproduce complex propagation patterns such as spiral waves with a limited number of degrees of freedom. Moreover, the method has been proven to be accurate in reconstructing solutions with thin layers [29], other than being able to control numerical dissipation and dispersion [15, 20]. In this respect, here we study the properties of the solution in terms of velocity and dispersion of the transmembrane potential front wave. In [38] a similar study was performed only for the monodomain equations.

This paper is structured as follows. First, in order to make it as self-contained as possible, we recall some fundamentals of cardiac physiology in Section 2. Section 3 focuses on the microscopic and macroscopic models of the human electrophysiology. In Section 4, we present the numerical approximation of the bidomain equations, which is based on the isogeometric concept for the spatial discretization and on a splitting scheme – according to which the microscopic ionic model and the bidomain equations are solved separately – for the time discretization. In Section 5, we aim at evaluating the effects of IGA on the properties of the potential front by solving the bidomain equations on simple benchmark geometries. In Section 6, a realistic simulation of the electrophysiology on both atria is presented. Finally, in Section 7 conclusions follow.

2. Principles of cardiac electrophysiology

The contraction of the cardiac muscle is initiated by electric phenomena occurring at the microscopic spatial and temporal scales [32, 42]. Thanks to an external electric stimulation originated at the sinoatrial node, cardiac muscular cells (the cardiomyocytes) undergo a process called action potential, featuring the evolution of the difference of electric potential across the cellular membrane (transmembrane potential) along the heartbeat; this is caused by the flow of Na^+, K^+, Cl^-, and Ca^{2+} ions from the intra- to the extracellular space and vice-versa. In particular, the variation of calcium concentration Ca^{2+} in the intracellular space occurring during the action potential determines the mechanical reaction of the contractile units (the sarcomeres) forming the cardiac cell. Therefore, the calcium concentration is the output of interest when modeling the mechano-chemical coupling in cardiomyocytes; we refer the reader to [47] for examples of simulations of an individual cardiac cell contraction based on the so-called active-strain approach, or to [27] for an example of coupling between the electrophysiology and the mechanics of the heart at the macroscopic scale.

Cardiomyocytes feature a cylindrical shape and are organized along preferred directions, called fibers. The electric stimulation passes from one cardiac cell to the surrounding ones because of the

gap junctions located at the binding sites of adjacent cells. The higher density of gap junctions in the longitudinal direction (compared to the transversal direction) determines a faster conduction of the signal and a subsequent stronger mechanical reaction [37] along the fiber direction. Patient specific fibers fields are nowadays available from MRI images at both te endo- and epi-cardio. It is still problematic, however, to reconstruct the internal sheetlet orientation with non-invasive imaging procedures; this information is necessary to realistically predict the propagation of the potential front through numerical models in three-dimensional geometries [46]. In this paper, the passage of ions from cell to cell in the cardiac tissue is modeled by the bidomain equations, which will be presented in Section 3.2 and will be used for the numerical simulations in Sections 5 and 6.

As previously noted, the electric excitation of the heart starts within the right atrium at the sinoatrial node – which is often called the natural pacemaker of the heart because of the ability of its special cells to autonomously excite themselves – and travels across the atrial cardiac tissue. The two atria are mutually electrically isolated; the signal travels from the right to the left atrium through four muscular bundles [48], the most important being the Bachmann's bundle (primary connection). When the excitation front reaches the atrioventricular node located in the right atrium, the signal is transmitted from the atria to the ventricles after a delay of about 100 ms as it travels along the bundle of His and Purkinje fibers. Such delay is important to establish the synchronized contraction of atria and ventricles and to determine the cardiac rythm. For more on the role of Purkinje fibers and the mechanisms leading to their activation, we refer the reader to [54].

3. Mathematical modeling of cardiac electrophysiology

3.1. Ionic membrane models

Ionic membrane models describe the dynamics of ionic species across the cellular membrane of a single-cell system and the subsequent variation of the transmembrane potential. They represent an extension to cardiac cells of the Hodgkin-Huxley formalism [30], which was originally proposed for modeling the action potential in neurons of giant squids. Ionic membrane models account for the variation of the transmembrane potential v, defined as the difference between the intra- and extracellular potentials u_i and u_e, one or more recovery variables and possibly concentration variables of the ionic species. The recovery or gating variables model the behavior of the cellular membrane, in particular the opening and closing of the ionic channels distributed over the surface of the cardiomyocytes; each of these channels is associated with the flow across the membrane of a particular ionic species. In the following, we denote with $\mathbf{w}$ a vector containing n_w recovery and ionic concentration variables. For a system composed by a single cell, any ionic membrane model can be written for $t \in (0, T)$ as

$$\begin{aligned} \frac{\partial v}{\partial t} &= H(v, \mathbf{w}) + I^s, \\ \frac{\partial \mathbf{w}}{\partial t} &= \mathbf{F}(v, \mathbf{w}), \end{aligned}$$

with the initial conditions $v = v_{\text{in}}$ and $\mathbf{w} = \mathbf{w}_{\text{in}}$. The terms $H(v, \mathbf{w})$ and $\mathbf{F}(v, \mathbf{w})$ depend on the chosen ionic membrane model and I^s is an externally applied electric stimulus. The evolution of v and $\mathbf{w}$ are used, in the bidomain equations, to model the passage of ions from the intra- to the extracellular space through the ionic current per unit surface $I_{ion}(v, \mathbf{w})$.

The literature on the available models is quite wide; we refer the reader to, e.g., [11] and [50] for an overview. Phenomenological models [50] describe the action potential without taking into account the physiological mechanisms that lead to the variation of the transmembrane potential. Among the others, we recall the FitzHug-Nagumo [23] and the Roger-McCulloch models [44]; we use the latter to model the electrophysiology of slabs of cardiac tissue in our numerical simulations presented in Section 5.

The Roger-McCulloch ionic membrane model considers the following equations for the transmembrane potential v and the unique recovery variable w:

$$\begin{aligned} \frac{dv}{dt} &= -\left[Gv\left(1 - \frac{v}{v_{\text{th}}}\right)\left(1 - \frac{v}{v_{\text{p}}}\right) + \eta_1 v w \right] + I^s, \\ \frac{dw}{dt} &= \eta_2 \left(\frac{v}{v_p} - \eta_3 w \right), \end{aligned} \tag{1}$$

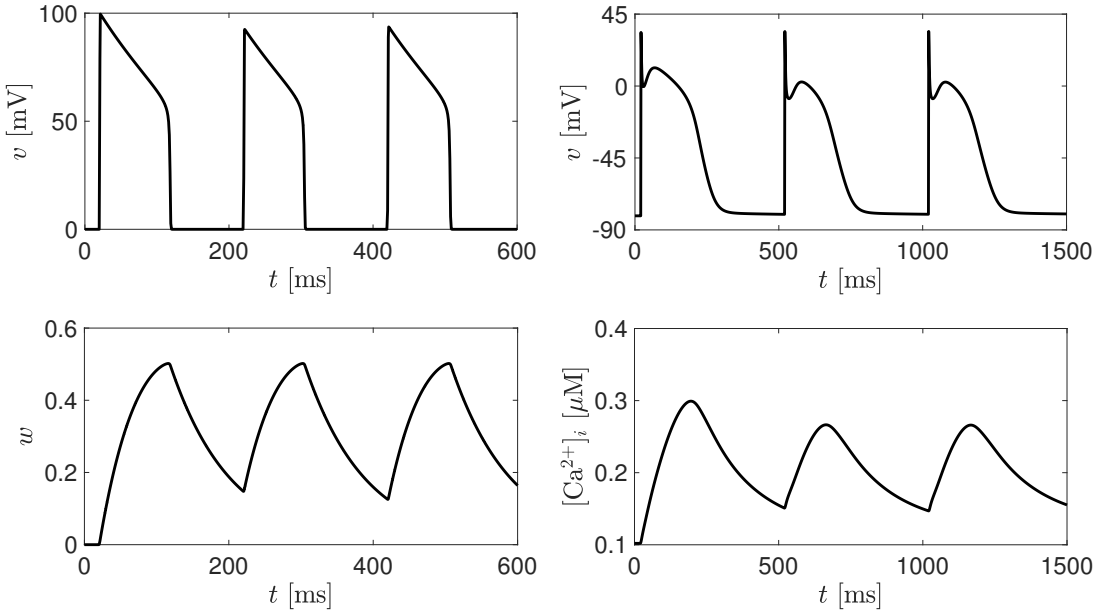

(a) Roger-McCulloch (b) Courtemanche-Ramirez-Nattel

Figure 1: On the left, transmembrane potential v and recovery variable w (which serves as a surrogate of $[\mathrm{Ca}^{2+}]_\mathrm{i}$) over three heartbeats obtained by the Roger-McCulloch model by applying a constant stimulus $I_\mathrm{app} = 50\,\mathrm{mA}$ for 1 ms initiated at $t = 20\,\mathrm{ms}$, $t = 220\,\mathrm{ms}$ and $t = 420\,\mathrm{ms}$. The ODE system (1) has been discretized by using the Forward Euler method with $\Delta t = 1 \times 10^{-3}\,\mathrm{ms}$. The values of the parameters are: $v_\mathrm{th} = 13\,\mathrm{mV}$, $v_\mathrm{p} = 100$ mV, $G = 1.5\,\mathrm{ms}^{-1}$, $\eta_1 = 4.4\,\mathrm{ms}^{-1}$, $\eta_2 = 0.012$ and $\eta_3 = 1$. On the right, transmembrane potential v and the intracellular calcium concentration $[\mathrm{Ca}^{2+}]_\mathrm{i}$ over three heartbeats computed by using the CRN model; a constant stimulus $I_\mathrm{app} = 80\,\mathrm{mA}$ has been applied for 1 ms at $t = 20\,\mathrm{ms}$, $t = 520\,\mathrm{ms}$ and $t = 1020\,\mathrm{ms}$. The solution is computed by using the Forward Euler method with $\Delta t = 1 \times 10^{-3}\,\mathrm{ms}$. Different scales on the axes are employed.

for $t \in (0, T)$. The ionic current per unit surface I_{ion} is then linked to the transmembrane potential by the relation $I_{ion} = -C_m dv/dt$, where C_m is the capacitance of the membrane and the negative sign comes from the convention of considering as positive the currents travelling from the intra- to the extracellular space. Fig. 1 (left) shows the evolution of v and w when a single cell system described by the Roger-McCulloch model is stimulated with a constant current I_app for 1 ms applied every 200 ms to simulate three heartbeats. With our choice of model parameters, the shape of the action potential is a rough approximation of the physiological action potential. Moreover, the resting and peak value of the transmembrane potential are not physical, as in cardiac cells v varies between around $-85\,\mathrm{mV}$ and $30\,\mathrm{mV}$. Hence, in order to get physiological values of the transmembrane potential, the solution of the Roger-McCulloch model must be conveniently rescaled. In this paper, as we employ this ionic model only on benchmark problems targeted to the analysis of the accuracy of the solutions obtained with IGA, we do not rescale the transmembrane potential.

Both first and second generation models [50] provide descriptions of the processes occurring in the cells and the currents associated with the flow of ionic species across the membrane. Commonly used second generation models are e.g. the two Luo-Rudy [35, 36] and the Bueno-Orovio [4] models. We refer the reader to [9] and [49] for applications of the phase I Luo-Rudy and the Bueno-Orovio models to the bidomain equations, respectively. In this paper, we focus on the model proposed by Courtemanche, Ramirez and Nattel [18] (CRN in the following), which is instead well-suited and tuned for modeling the electrophysiology of atrial cells. The CRN model takes into account 15 recovery variables and the intracellular concentrations of 3 ionic species, namely $[\mathrm{K}^+]_i$, $[\mathrm{Na}^+]_i$ and $[\mathrm{Ca}^{2+}]_i$, as well as the concentration of calcium during the uptake and release compartments of the sarcoplasmic reticulum $[\mathrm{Ca}^{2+}]_\mathrm{up}$ and $[\mathrm{Ca}^{2+}]_\mathrm{rel}$. The ionic current is determined by the action of 12 currents

$$I_{ion} = I_\mathrm{Na} + I_\mathrm{K1} + I_\mathrm{to} + I_\mathrm{Kur} + I_\mathrm{Kr} + I_\mathrm{Ks} + I_\mathrm{Ca,L} + I_\mathrm{p,Ca} + I_\mathrm{NaK} + I_\mathrm{NaCa} + I_\mathrm{b,Na} + I_\mathrm{b,Ca},$$

each of them being associated with the flow of specific ionic species across the cellular membrane. We refer the reader to [18] for the complete description of the model and the governing equations. Fig. 1 (right) shows the evolution of v and $[\mathrm{Ca}^{2+}]_i$ computed with the CRN model. In our formulation we consider a slight modification of the formulation presented in [18]: the right hand-sides of the equations

corresponding to $d[\mathrm{Na}^+]_i/dt$, $d[\mathrm{K}^+]_i/dt$ and $d[\mathrm{Ca}^{2+}]_i/dt$ are scaled by a factor $A_{\mathrm{cap}} = 2(2\pi r^2 + 2\pi r L)$ (where r and L are the radius and length of the cylindrical cell), i.e. the capacitive surface area of the cell. We took inspiration from [36] for the definition of this term.

3.2. The bidomain equations

We consider the bidomain equations [11, 28] for modeling the propagation of the electric signal and excitation front in the cardiac tissue. In the bidomain model, the region Ω occupied by the cardiac tissue is assumed to be a continuum composed by two inter-penetrating domains [39], the intra- and the extracellular spaces. Each point $\mathbf{x} \in \Omega$ is associated with the intracellular potential u_i, the extracellular potential u_e, and to the transmembrane potential $v = u_i - u_e$.

As described in Section 2, the heart is mostly composed of cardiomyocytes: these cells are organized in fibers and each of them is characterized by the ability to exchange ions with the surrounding ones. The anisotropic behavior of the tissue due to the different velocities of conduction longitudinally and transversally to the fibers directions is mathematically modeled by tensors $D_{i,e}(\mathbf{x})$, commonly defined in the three-dimensional case by [11]

$$D_{i,e}(\mathbf{x}) := \sigma_l^{i,e}(\mathbf{x})\widehat{\mathbf{a}}_l(\mathbf{x})\widehat{\mathbf{a}}_l^T(\mathbf{x}) + \sigma_t^{i,e}(\mathbf{x})\widehat{\mathbf{a}}_t(\mathbf{x})\widehat{\mathbf{a}}_t^T(\mathbf{x}) + \sigma_n^{i,e}(\mathbf{x})\widehat{\mathbf{a}}_n(\mathbf{x})\widehat{\mathbf{a}}_n^T(\mathbf{x}), \tag{2}$$

where $\widehat{\mathbf{a}}_l(\mathbf{x}) : \Omega \to \mathbb{R}^3$, $\widehat{\mathbf{a}}_t(\mathbf{x}) : \Omega \to \mathbb{R}^3$, $\widehat{\mathbf{a}}_n(\mathbf{x}) : \Omega \to \mathbb{R}^3$ are unit vectors forming an orthonormal basis at the point $\mathbf{x}$, $\widehat{\mathbf{a}}_l$ being parallel to the local fibers direction, $\widehat{\mathbf{a}}_t$ being perpendicular to $\widehat{\mathbf{a}}_l$ and laying on the plane tangential to the fibers, and $\widehat{\mathbf{a}}_n$ being perpendicular to both $\widehat{\mathbf{a}}_l$ and $\widehat{\mathbf{a}}_t$; $\sigma_{l,t,n}^{i,e}$ are the associated conductivities. When dealing with surfaces embedded in three dimensions, $\widehat{\mathbf{a}}_n$ can be identified as the local normal vector to the surface. For a surface, $\sigma_n^{i,e} = 0$. Defining the conductivity tensor through the orthonormal basis presented above is motivated by the laminar organization of the cardiac tissue in muscle sheets [34].

Given all the assumptions above – whose physiological suitability is analyzed in [53] – we are ready to present the bidomain equations in parabolic-elliptic formulation [3, 11], for a surface Ω embedded in $\mathbb{R}^d$

$$\begin{aligned}
&c_m\frac{\partial v}{\partial t} - \nabla_\Omega\cdot(D_i\nabla_\Omega v) - \nabla_\Omega\cdot(D_i\nabla_\Omega u_e) + \chi I_{ion}(v,\mathbf{w}) = I_i^s && \text{in } \Omega\times(0,T),\\
&-\nabla_\Omega\cdot(D_i\nabla_\Omega v) - \nabla_\Omega\cdot((D_i+D_e)\nabla_\Omega u_e) = I_e^s + I_i^s && \text{in } \Omega\times(0,T),\\
&\frac{\partial \mathbf{w}}{\partial t} = \mathbf{F}(v,\mathbf{w}), && \text{in } \Omega\times(0,T),\\
&\mathbf{n}^T D_i\nabla_\Omega(v+u_e) = 0 && \text{on } \partial\Omega\times(0,T),\\
&\mathbf{n}^T(D_i+D_e)\nabla_\Omega u_e + \mathbf{n}^T D_i\nabla_\Omega v = 0 && \text{on } \partial\Omega\times(0,T),\\
&v = v_{\mathrm{in}}, \quad \mathbf{w} = \mathbf{w}_{\mathrm{in}}, && \text{in } \Omega\times\{0\},
\end{aligned} \tag{3}$$

where $c_m = \chi C_m$, χ being the area of cell membrane per tissue volume and C_m being the capacitance of the membrane, and $I_{i,e}^s$ are the applied external currents. The differential operator ∇_Ω stands for the surface gradient operator: $\nabla_\Omega\phi : \Omega \to \mathbb{R}^d$ for any $\phi \in C^1(\Omega)$, while the differential operator $\nabla_\Omega\cdot$ indicates the surface divergence operator: $\nabla_\Omega\cdot\boldsymbol{\phi} : \Omega \to \mathbb{R}$ for any $\boldsymbol{\phi} \in [C^1(\Omega)]^d$. We remark that, for any function space $\mathcal{S}$, we indicate with $[\mathcal{S}]^d$ the space of functions taking values in $\mathbb{R}^d$ with each component belonging to $\mathcal{S}$. Using the same notation introduced in Section 3.1, we denote with $\mathbf{w}$ the vector containing the recovery and concentration variables, with $I_{ion}(v,\mathbf{w})$ the ionic current and with $\mathbf{F} : \mathbb{R}\times\mathbb{R}^{n_w} \to \mathbb{R}^{n_w}$ the evolution law of the recovery variable, which is prescribed by the ionic membrane model of choice. Since the domain Ω is assumed to be electrically isolated, homogeneous Neumann boundary conditions are set on $\partial\Omega$, for $t \in (0,T)$.

Under the hypotheses that the tensors $D_{i,e}$ are positive definite matrices (uniformly with respect to $\mathbf{x}$), that the domain Ω has a Lipschitz boundary $\partial\Omega$, that the extracellular potential u_e has null average on Ω, and under regularity assumptions over I_{ion}, $\mathbf{F}$, and $I_{i,e}^s$, the bidomain equations admit a unique solution [3]. These hypotheses are sufficient to show the well-posedness of the bidomain equations for simple ionic membrane models, such as the FitzHug-Nagumo and the Roger McCulloch models (see Section 3.1), provided that Ω, $D_{i,e}$, u_e and $I_{i,e}$ satisfy the necessary assumptions in [3]. Among the regularity conditions mentioned above, we recall the compatibility condition on the applied currents

$$\int_\Omega (I_i^s + I_e^s)\, d\mathbf{x} = 0, \tag{4}$$

which must be satisfied for all $t \in (0,T)$.

With the purpose of presenting the weak formulation of the bidomain equations, we introduce the function spaces $\mathcal{V} = H^1(\Omega), \mathcal{W} = L^2(\Omega)$ and $\mathcal{U}_e = \mathcal{V}/\mathbb{R}$, the latter being the space of functions of $\mathcal{V}$ with zero mean value on Ω. Moreover, we consider the following bilinear forms

$$a(\phi,\psi) := \left((D_i + D_e)\nabla_\Omega\phi, \nabla_\Omega\psi\right),$$
$$a_i(\phi,\psi) := ((D_i\nabla_\Omega\phi), \nabla_\Omega\psi),$$

for all $\phi, \psi \in \mathcal{V}$. We denote with $(\cdot,\cdot)$ the usual L^2 inner product. The weak formulation of Eq. (3) is derived by multiplying the first three equations by test functions $\widetilde{v} \in \mathcal{V}$, $\widetilde{u}_e \in \mathcal{U}_e$ and $\widetilde{\mathbf{w}} \in [\mathcal{W}]^{n_w}$ respectively and by integrating on Ω. Under the assumptions that $v_{\text{in}} \in \mathcal{W}$, $\mathbf{w}_{\text{in}} \in [\mathcal{W}]^{n_w}$, and that $I^s_{i,e} \in L^2(\Omega \times (0,T))$ satisfy Eq. (4), the weak formulation of the bidomain equations [25] reads

(W1) find $v \in L^2(0,T;\mathcal{V})$, $u_e \in L^2(0,T;\mathcal{V})$, $\mathbf{w} \in L^2(0,T;[\mathcal{W}]^{n_w})$ and $\lambda \in L^2(0,T;\mathbb{R})$ such that, $\forall t \in (0,T)$,

$$\begin{aligned}
&c_m \frac{d}{dt}(v,\widetilde{v}) + a_i(v,\widetilde{v}) + a_i(u_e,\widetilde{v}) + \chi(I_{ion}(v,\mathbf{w}),\widetilde{v}) = (I^s_i,\widetilde{v}) && \forall \widetilde{v} \in \mathcal{V},\\
&a_i(v,\widetilde{u}_e) + a(u_e,\widetilde{u}_e) + (\lambda,\widetilde{u}_e) = (I^s_i + I^s_e,\widetilde{u}_e) && \forall \widetilde{u}_e \in \mathcal{V},\\
&\frac{d}{dt}(\mathbf{w},\widetilde{\mathbf{w}}) = (\mathbf{F}(v,\mathbf{w}),\widetilde{\mathbf{w}}) && \forall \widetilde{\mathbf{w}} \in [\mathcal{W}]^{n_w},\\
&(u_e,\widetilde{\lambda}) = 0 && \forall \widetilde{\lambda} \in \mathbb{R},
\end{aligned} \tag{5}$$

with $\partial v/\partial t \in L^2(0,T;\mathcal{V})$ and $\partial \mathbf{w}/\partial t \in L^2(0,T;[\mathcal{W}]^{n_w})$.

For practical reasons, we have decided not to impose the condition of null mean value of u_e directly on the trial space, but instead to introduce a suitable Lagrange multiplier λ.

4. Numerical approximation of the bidomain equations

4.1. Space discretization

As we have seen, the bidomain equations in parabolic-elliptic formulation consist of two PDEs, the first in Eq. (3) being parabolic and the second elliptic; these two equations are coupled with a system of ODEs which models the evolution of the recovery variables and ionic concentration $\mathbf{w}$. This variable accounts for the microscopic events leading to the onset of the action potential – such as the opening or closing of the ionic channels of the different species – and contributes to the term $I_{ion}(v,\mathbf{w})$ in the parabolic equation. Different strategies for dealing with the discretization of the PDEs and the system of ODEs have been devised; see e.g. [33, 38] for the analogous case of the monodomain equations. A first possible approach, called "nodal interpolation", consists in defining a function space for the recovery variables $\mathbf{w}$ – often built by means of the same basis functions that are used for approximating v and u_e – and discretizing the ODEs by following a standard Galerkin method [41]. The second approach, called "Gaussian integration", consists in approximating the ODEs only at the Gauss quadrature nodes. In this paper, we choose to follow the latter strategy.

We discretize the variational space $\mathcal{V}$ by means of B-splines and NURBS-based IGA [16, 31] in the framework of the Galerkin method. The main idea of IGA is to consider the same basis functions for representing first the geometry and then for constructing the trial function space for the solution. As already mentioned, the geometries we consider in this work are surfaces: see e.g. [21] and [1] for examples of solutions of surface PDEs using IGA. Given a knot vector $\boldsymbol{\Xi} = \{\xi_1, \ldots, \xi_N\}$, we denote $\{\widehat{R}^p_j\}_{j=1}^n$ the set of B-spline piecewise polynomial basis functions of polynomial degree p generated by means of the Cox-De Boor recursion formula [19] applied to $\boldsymbol{\Xi}$; it holds that $N = n + p + 1$. We consider only open knot vectors, i.e. knot vectors in which the first and last knots have the same multiplicity. The knot vector $\boldsymbol{\Xi}$ determines both the polynomial degree p of the piecewise polynomials and the regularity (i.e. the number of continuous derivatives) of the basis functions across the knots. The number of repeated knots at the extrema of the interval determines the degree of the polynomials; in particular, if $\xi_1 = \xi_2 = \ldots = \xi_{p+1}$ and $\xi_{N-p} = \xi_{N-p+1} = \ldots = \xi_N$, the resulting B-spline basis functions have polynomial degree p. The regularity of the basis functions is instead determined by the multiplicity of the internal knots. Namely, given an internal knot ξ_i with multiplicity m_i, the resulting basis functions are C^{p-m_i}-continuous across ξ_i. Fig. 2 shows examples of B-spline basis functions.

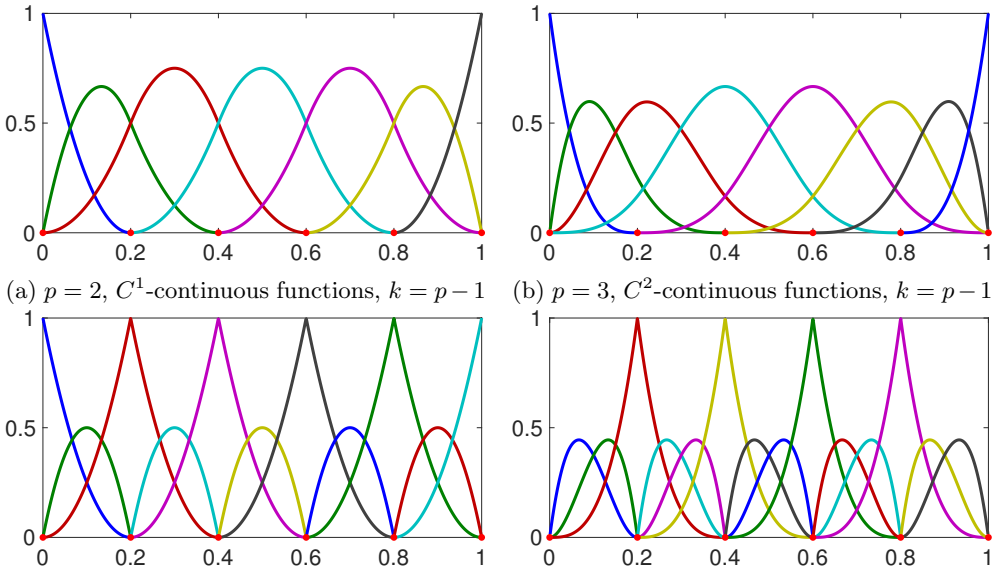

(a) $p = 2$, C^1-continuous functions, $k = p - 1$ (b) $p = 3$, C^2-continuous functions, $k = p - 1$

(c) $p = 2$, C^0-continuous functions, $k = 0$ (d) $p = 3$, C^0-continuous functions, $k = 0$

Figure 2: B-spline basis functions with different polynomial degree and regularity across the elements. The knot vector generating each basis is constructed by using the set of knots $\{\{0\}^{p+1}, \{0.2\}^{p-k}, \{0.4\}^{p-k}, \{0.6\}^{p-k}, \{0.8\}^{p-k}, \{1\}^{p+1}\}$, where p is the polynomial degree and k is the global continuity of the basis.

NURBS are generated from B-splines by considering a set of weights $\{w_i\}_{i=1}^n$ and by defining, for $j = 1, \dots, n$,

$$\widehat{N}_j^p := \frac{\widehat{R}_j^p w_j}{W},$$

where $W = \sum_{j=1}^n \widehat{R}_j^p w_j$ is the weighting function. In this work, we assume $w_j \in \mathbb{R}$ and $w_j > 0$ for each $j = 1, \dots, n$. Multivariate B-spline and NURBS basis functions are obtained by means of the tensor product of sets of univariate basis functions. In the following, we will simply denote $\{\widehat{N}_j\}_{j=1}^n$ multivariate NURBS basis functions, and $\mathbf{s} \in \widehat{\Omega}$ a generic point in the parametric domain, namely the support of the multivariate basis functions. The use of NURBS is mainly motivated by geometrical needs. As a matter of fact, since B-splines are piecewise polynomials, they can not exactly represent common geometries such as circles, cylinders, and conic sections in general, which can be instead represented by choosing appropriate weights to be associated with the B-splines [51]. We refer the reader to [19] and [16] for details on the properties of B-splines and NURBS basis functions, to [51] for details on the accuracy of NURBS basis functions under h-, p- and k-refinement, and to [17, 31] for a complete overview of IGA.

Let us assume that the computational domain Ω is a surface in $\mathbb{R}^3$. Moreover, let us assume that there exist a set of bivariate NURBS basis functions $\{\widehat{N}_j\}_{j=1}^n$ and an invertible mapping $\mathbf{x} : \widehat{\Omega} \to \Omega$ in the form

$$\mathbf{x}(\mathbf{s}) := \sum_{j=1}^n \widehat{N}_j(\mathbf{s}) \mathbf{B}_j$$

from the parametric domain $\widehat{\Omega}$ to the physical domain Ω. The vectors $\mathbf{B}_j \in \mathbb{R}^3$ are called control points. By following the isogeometric concept, we construct a finite dimensional function space $\mathcal{V}^h \subset \mathcal{V}$ spanned by the functions $\{N_j\}_{j=1}^n$, where $N_j = \widehat{N}_j \circ \mathbf{x}^{-1}$, i.e. $\mathcal{V}^h = \mathcal{V} \cap \text{span}\{N_j\}_{j=1}^n$. We consider, for all $t \in (0, T)$, $v^h(t) \in \mathcal{V}^h$ and $u_e^h(t) \in \mathcal{V}^h$ defined by

$$\begin{aligned} v^h(t) &:= \sum_{j=1}^n V_j(t) N_j, \\ u_e^h(t) &:= \sum_{j=1}^n U_j(t) N_j, \end{aligned} \tag{6}$$

which approximate v and u_e respectively; the explicit dependence on the spatial variable has been

omitted. The parabolic and elliptic equations in (5) can be projected onto $\mathcal{V}^h$, yielding, for all $t \in (0,T)$,

$$\begin{aligned} &c_m \frac{d}{dt}\left(v^h(t), \widetilde{v}^h\right) + a_i(v^h(t), \widetilde{v}^h) + a_i(u_e^h(t), \widetilde{v}^h) + \chi(I_{ion}(v^h(t), \mathbf{w}(t)), \widetilde{v}^h) = (I_i^s(t), \widetilde{v}^h), \\ &a_i(v^h(t), \widetilde{u}_e^h) + a(u_e^h(t), \widetilde{u}_e^h) + (\lambda^h(t), \widetilde{u}_e^h) = (I_i^s(t) + I_e^s(t), \widetilde{u}_e^h), \end{aligned} \tag{7}$$

for any $\widetilde{v}^h \in \mathcal{V}^h$ and for any $\widetilde{u}_e^h \in \mathcal{V}^h$. The initial condition $v^h(0) = v_{\text{in}}^h$, $v_{\text{in}}^h = \sum_{j=1}^n v_{\text{in},j} N_k$ is a suitable projection (e.g. L^2-projection) of the initial data onto $\mathcal{V}^h$ and $\mathbf{w}(t) \in \mathcal{W}$ is, for the time being, assumed to be given. Eq. (7) holds for any $\widetilde{v}^h \in \mathcal{V}^h$ and $\widetilde{u}_e^h \in \mathcal{V}^h$ and, in particular, for $N_l \in \mathcal{V}^h$ with $l = 1, \dots, n$. By substituting $\widetilde{v}^h$ and $\widetilde{u}_e^h$ with N_l and by expanding v^h and u_e^h in the linear terms on the basis as in Eq. (6), we find, for $t \in (0,T)$ and $l = 1, \dots, n$,

$$\begin{aligned} &c_m \sum_{j=1}^n \frac{d}{dt} V_j(t) m_{lj} + \sum_{j=1}^n V_j(t) r_{lj} + \sum_{j=1}^n U_j(t) r_{lj} + \chi(I_{ion}(v^h(t), \mathbf{w}(t)), N_l) = (I_i^s(t), N_l), \\ &\sum_{j=1}^n V_j(t) r_{lj} + \sum_{j=1}^n U_j(t) k_{lj} + b_l \lambda^h(t) = (I_i^s(t) + I_e^s(t), N_l), \end{aligned} \tag{8}$$

with $v_j(0) = v_{\text{in},j}$ for $j = 1, \dots, n$, $m_{lj} = (N_j, N_l)$, $k_{lj} = a(N_j, N_l)$, $r_{lj} = a_i(N_j, N_l)$, and $b_l = \int_\Omega N_l \, d\mathbf{x}$. By introducing the mass matrix $(M)_{kj} = m_{kj}$ and the stiffness matrices $(K)_{lj} = k_{lj}$ and $(R)_{lj} = r_{lj}$, Eq. (8) can be compactly rewritten in system form for $t \in (0,T)$ as

$$\begin{aligned} &c_m M \frac{d}{dt}\mathbf{V}(t) + R\mathbf{V}(t) + R\mathbf{U}(t) + \chi \mathbf{I}_{ion}(v^h(t), \mathbf{w}(t)) = \mathbf{I}_i^s(t), \\ &R\mathbf{V}(t) + K\mathbf{U}(t) + \mathbf{B}\lambda^h(t) = \mathbf{I}_i^s(t) + \mathbf{I}_e^s(t), \end{aligned} \tag{9}$$

where $(\mathbf{I}_{ion}(v^h(t), \mathbf{w}(t)))_j = (I_{ion}(v^h(t), \mathbf{w}(t)), N_j)$, $(\mathbf{V}(t))_j = v_j(t)$, $(\mathbf{U}(t))_j = u_j(t)$, $(\mathbf{I}_{i,e}^s(t))_j = (I_{i,e}^s(t), N_j)$, $(\mathbf{B})_j = b_j$ and $(\mathbf{V}(0))_j = (\mathbf{V}_{\text{in}}) = v_{\text{in},j}$. With this notation, the null mean value condition ($\int_\Omega u_e^h \, d\mathbf{x} = 0$) on the external potential simply reads

$$\mathbf{B}^T \mathbf{U}(t) = 0.$$

Let us now consider the computation of the nonlinear term $\mathbf{I}_{ion}(v^h(t), \mathbf{w}(t))$. The parametric space and – consequently – the physical space are partitioned into mesh elements that are determined by the subdivision in knots of the intervals (ξ_1, ξ_N) in the parametric directions. Let us suppose that $\Omega = \bigcup_{i=1}^{n_{el}} E_i$, i.e. that the domain is composed by elements E_i with $i = 1, \dots, n_{el}$. We notice that the l^{th} component of the vector $\mathbf{I}_{ion}(v^h(t), \mathbf{w}(t))$ is computed as

$$(I_{ion}(v^h(t), \widetilde{\mathbf{w}}(t)), N_l) = \int_\Omega I_{ion}(v^h(t), \widetilde{\mathbf{w}}(t)) N_l \, d\mathbf{x} = \sum_{i=1}^{n_{el}} \int_{E_i} I_{ion}(v^h(t), \widetilde{\mathbf{w}}(t)) N_l \, d\mathbf{x}. \tag{10}$$

We choose to approximate integrals in the weak formulation by means of Gauss-Legendre quadrature formulas with $s = (p+1)(q+1)$ quadrature nodes (p and q being the order of the piecewise polynomials in the two parametric directions). Let $\boldsymbol{\phi}_i : (-1,1)^2 \to E_i$ be the transformation from the square reference element for the Gauss-Legendre quadrature formulas in two dimensions to the i^{th} element, and let $\{\overline{\mathbf{x}}_{\text{G}}^j\}_{j=1}^s$ and $\{\omega_{\text{G}}^j\}_{j=1}^s$ be the corresponding quadrature nodes and weights. The integral in Eq. (10) is numerically computed as

$$\int_\Omega I_{ion}(v^h(t), \widetilde{\mathbf{w}}(t)) N_l \, d\mathbf{x} \approx \sum_{i=1}^{n_{el}} \sum_{j=1}^{s} |\det(J_i)| \omega_G^j \left(I_{ion}(v^h(t, \mathbf{x}_G^{i,j}), \widetilde{\mathbf{w}}(t, \mathbf{x}_G^{i,j})) N_l(\mathbf{x}_G^{i,j}) \right), \tag{11}$$

where $J_i = \partial \boldsymbol{\phi}_i / \partial \overline{\mathbf{x}}$ is the Jacobian matrix of $\boldsymbol{\phi}_i$ with respect to the reference spatial variable, and $\mathbf{x}_{\text{G}}^{i,j} = \boldsymbol{\phi}_i^{-1}(\overline{\mathbf{x}}_{\text{G}}^j)$ is the j^{th} Gauss quadrature node in the i^{th} element of the mesh. It follows that, in order to compute the term $\mathbf{I}_{ion}$ contributing to the first equation in Eq. (9), it is sufficient to know the ionic current at the quadrature nodes $\mathbf{x}_{\text{G}}^{i,j}$. Therefore, instead of constructing a function space for the recovery variables $\mathbf{w}$, we define the vector $\mathbf{W}(t) : (0,T) \to \mathbb{R}^{n_w \times n_{el} \times s}$, which stores the values of the recovery variables at every Gauss quadrature node. With an abuse of notation, we write the system of ODEs describing the evolution of $\mathbf{W}(t)$ for $t \in (0,T)$ as

$$\frac{d}{dt}\mathbf{W}(t) = \mathbf{F}(\mathbf{V}(t), \mathbf{W}(t)), \tag{12}$$

with $\mathbf{W}(0) = \mathbf{W}_{\text{in}}$. Eq. (12) is to be intended in the following sense. The i^{th} component of $\mathbf{W}(t)$, i.e. $W_i(t)$ is associated with a particular Gauss quadrature node in the computational mesh. The evolution of the recovery and concentration variables in such point is determined by the ionic membrane model and it is a function of $W_i(t)$ itself and of the value of $v^h(t)$ – or equivalently $\mathbf{V}(t)$, see Eq. (6) – in that quadrature point.

From Eq. (11) and based on the previous considerations, it follows that the approximation by means of the Gauss quadrature rule of the ionic current vector in Eq. (9) can be considered in terms of $\mathbf{V}(t)$ and $\mathbf{W}(t)$; therefore, we introduce the notation

$$\mathbf{I}_{ion}^h(\mathbf{V}(t), \mathbf{W}(t)) \approx \mathbf{I}_{ion}(v^h(t), \mathbf{w}(t)).$$

By combining Eqs. (9) and (12), we finally find the semi-discrete formulation of the bidomain equations

(W2) find $\mathbf{V}(t)$, $\mathbf{U}(t)$, $\mathbf{W}(t)$ and $\lambda^h(t)$ such that $\forall t \in (0, T)$

$$\begin{aligned}
&c_m M \frac{d}{dt}\mathbf{V}(t) + R\mathbf{V}(t) + R\mathbf{U}(t) + \chi \mathbf{I}_{ion}^h(\mathbf{V}(t), \mathbf{W}(t)) = \mathbf{I}_i^s(t),\\
&R\mathbf{V}(t) + K\mathbf{U}(t) + \mathbf{B}\lambda^h(t) = \mathbf{I}_i^s(t) + \mathbf{I}_e^s(t),\\
&\frac{d}{dt}\mathbf{W}(t) = \mathbf{F}(\mathbf{V}(t), \mathbf{W}(t)),\\
&\mathbf{B}^T\mathbf{U}(t) = 0,\\
&\mathbf{V}(0) = \mathbf{V}_{\text{in}}, \quad \mathbf{W}(0) = \mathbf{W}_{\text{in}}.
\end{aligned} \tag{13}$$

4.2. Time discretization

In order to obtain the fully discretized version of the semi-discrete problem (13), we consider a first order splitting scheme with semi-implicit treatment of the nonlinear terms. We refer the reader to [8, 11, 26] for other examples of split and/or staggered schemes applied to the bidomain equations.

We use the Backward Differentiation Formulas (BDF) [43] for the approximation of the time derivatives. Given an initial-value problem in the form $dy/dt = f(t, y)$ for $t \in (0, T)$ (with $y(0) = y_0$), let Δt be a timestep size such that $t_k = t_0 + k\Delta t$ and $y_k = y(t_k)$. The numerical approximation of the derivative dy/dt at the time t_{k+1} by a BDF scheme of order $\sigma \geq k - 1$ is given by

$$\frac{d}{dt}y(t_{k+1}) \approx \alpha_0 \frac{y_{k+1} - y_{k+1}^{\text{BDF}}}{\Delta t} = f(t, y_{k+1}), \tag{14}$$

where $y_{k+1}^{\text{BDF}} = -\sum_{j=1}^{\sigma}(\alpha_j/\alpha_0)y_{k+1-i}$ is a linear combination of the solutions at the previous steps, and $\alpha_j \in \mathbb{R}$ with $j = 0, \ldots, \sigma$ (with $\alpha_0 \neq 0$) are coefficients depending on the order of the method.

Eq. (14) is in general nonlinear as the right hand-side is evaluated in the unknown y_{k+1}. With the purpose of lowering the computational burden of the time discretization, we replace y_{k+1} at the right handside of Eq. (14) by an extrapolated value y_{k+1}^*, obtained by linear combination of the values y_j with $j = k, \ldots, k - (\sigma - 1)$ [6]. Specifically, we use the equal order extrapolation based on Gregory-Newton polynomials [24].

We use the notation $\mathbf{V}_k := \mathbf{V}(t_k)$, $\mathbf{U}_k := \mathbf{U}(t_k)$, $\mathbf{W}_k := \mathbf{W}(t_k)$ and $\lambda_k := \lambda^h(t_k)$ for denoting the variables of interest evaluated at the time instance t_k. The initial conditions on these variables are imposed by setting $\mathbf{V}_0 = \mathbf{V}_{\text{in}}$ and $\mathbf{W}_0 = \mathbf{W}_{\text{in}}$. For BDF schemes of order $\sigma > 1$, the first k steps with $k = -1, \ldots, -(\sigma - 1)$ are computed with lower order BDF schemes. The first order splitting scheme for the integration of Eq. (13) at the time instance t_{k+1} for any $k > 0$ consists of the following two steps:

1. given $\mathbf{V}_{k+1}^*$ and $\mathbf{W}_{k+1}^*$, namely the extrapolated values of $\mathbf{V}(t)$ and $\mathbf{W}(t)$ at the time instance t_{k+1}, Eq. (12) is discretized as

$$\mathbf{W}_{k+1} = \mathbf{W}_{k+1}^{\text{BDF}} + \frac{\Delta t}{\alpha_0}\mathbf{F}(\mathbf{V}_{k+1}^*, \mathbf{W}_{k+1}^*). \tag{15}$$

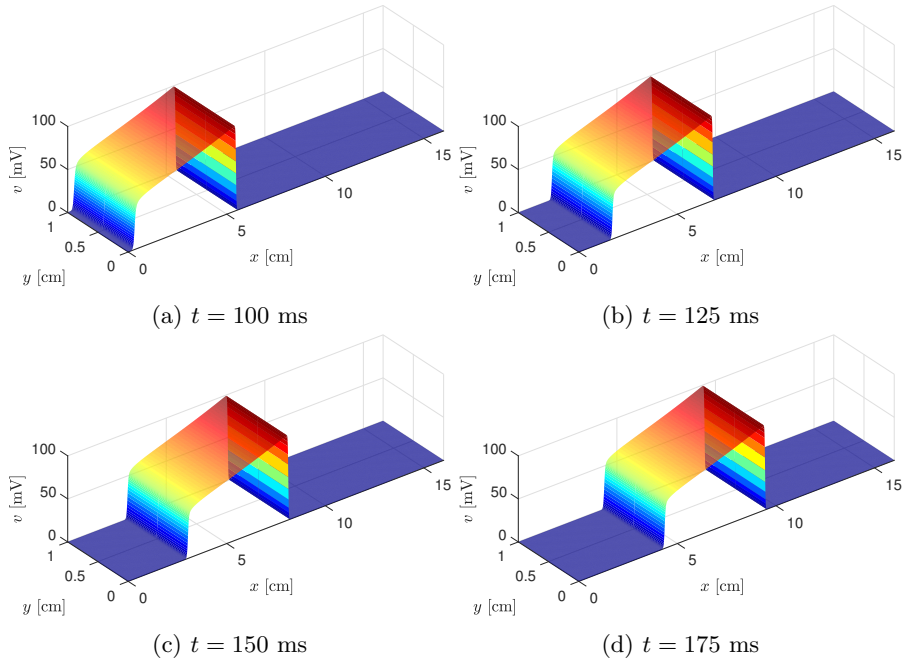

(a) $t = 100$ ms (b) $t = 125$ ms

(c) $t = 150$ ms (d) $t = 175$ ms

Figure 3: Three-dimensional representation of the front of the transmembrane potential v in the rectangular slab at different time instances, computed using P2/C1 basis functions and $1024 \times 64 = 65'536$ uniform elements ($h = 1.56 \times 10^{-2}$ cm).

2. given $\mathbf{W}_{k+1}$, the values $\mathbf{V}_{k+1}$, $\mathbf{U}_{k+1}$ and λ_{k+1} are found by solving

$$\begin{aligned} & c_m M \alpha_0 \frac{\mathbf{V}_{k+1} - \mathbf{V}_{k+1}^{\text{BDF}}}{\Delta t} + R\mathbf{V}_{k+1} + R\mathbf{U}_{k+1} + \chi \mathbf{I}_{ion}^h(\mathbf{V}_{k+1}^*, \mathbf{W}_{k+1}) = \mathbf{I}_{i,k+1}^s, \\ & R\mathbf{V}_{k+1} + K\mathbf{U}_{k+1} + \mathbf{B}\lambda_{k+1} = \mathbf{I}_{i,k+1}^s + \mathbf{I}_{e,k+1}^s, \\ & \mathbf{B}^T \mathbf{U}_{k+1} = 0, \end{aligned} \tag{16}$$

where $\mathbf{I}_{i,k+1}^s := \mathbf{I}_i^s(t_{k+1})$ and $\mathbf{I}_{e,k+1}^s := \mathbf{I}_e^s(t_{k+1})$.

Finally, we remark that the choice of updating the recovery variables first and then the transmembrane and the external potentials is arbitrary [26]. Another valid possibility would consist of inverting the order in which the two steps are performed. As a matter of fact, $\mathbf{V}_{k+1}$ and $\mathbf{U}_{k+1}$ could be computed first from Eq. (16) by replacing $\mathbf{W}_{k+1}$ with the extrapolated value $\mathbf{W}_{k+1}^*$; the recovery variable at the new timestep $\mathbf{W}_{k+1}$ could be then determined from Eq. (15) by replacing $\mathbf{V}_{k+1}^*$ with $\mathbf{V}_{k+1}$.

5. Numerical solution of benchmark problems in electrophysiology

In this section, we assess the properties of the numerical solution of the bidomain equations obtained by means of IGA based on B-splines, specifically using the discretization strategy outlined in Section 4. For all the following benchmark problems, we solve the bidomain equations with the Roger-McCulloch ionic membrane model that was introduced in Eq. (1). We assign the initial conditions $v_{\text{in}} = 0$ mV and $w_{\text{in}} = 0$ and we use the BDF scheme of order $\sigma = 2$ with $\Delta t = 0.05$ ms. We denote with P1/C0 the B-splines piecewise linear polynomial basis functions with discontinuous derivatives across the elements, with P2/C1 the B-splines piecewise quadratic polynomial basis functions with continuity of the first derivative across the elements, etc [21].

The geometries used for all the simulations in this section and Section 6 were generated with the NURBS package for MATLAB. The equations were solved by using isoGlib, a high performance C++ library specifically built for solving problems by means of NURBS-based IGA.

5.1. Transmembrane potential wave front propagation in a rectangular slab

We consider a rectangular slab $\Omega = (0, 16)\,\text{cm} \times (0, 1)\,\text{cm}$. The tissue is composed by fibers laid parallel to the longitudinal direction, i.e. $\widehat{\mathbf{a}} = \widehat{\mathbf{x}}$, and its physical properties – as well as the values

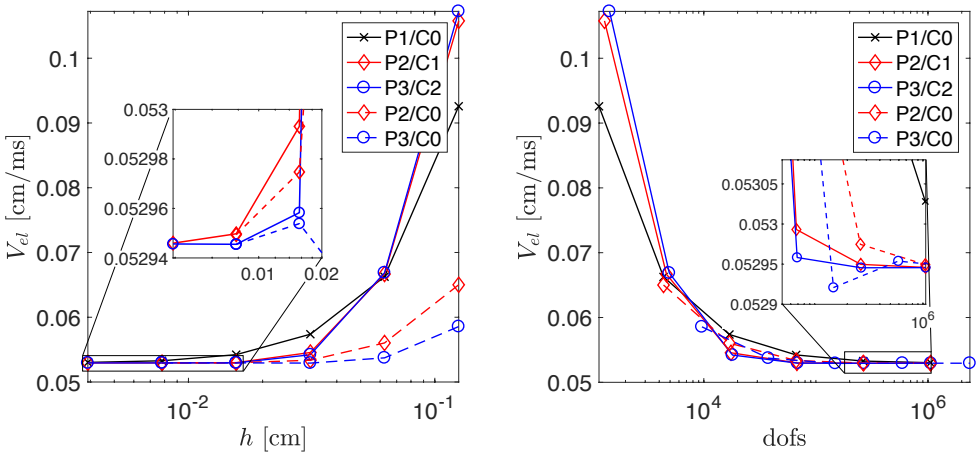

Figure 4: Convergence of the potential front velocity for different piecewise polynomial basis functions with respect to the element size h (on the left) and with respect to the number of degrees of freedom (on the right).

Material properties	$\sigma_l^i = 2.3 \cdot 10^{-3}\ \Omega^{-1}\text{cm}^{-1}$ $\sigma_l^e = 1.5 \cdot 10^{-3}\ \Omega^{-1}\text{cm}^{-1}$ $c_m = 1\ \text{mF cm}^{-3}$	$\sigma_t^i = 2.4 \cdot 10^{-4}\ \Omega^{-1}\text{cm}^{-1}$ $\sigma_t^e = 10^{-3}\ \Omega^{-1}\text{cm}^{-1}$ $\chi = 10^3\ \text{cm}^{-1}$
Roger-McCulloch parameters	$v_{\text{th}} = 13\ \text{mV}$ $v_{\text{p}} = 100\ \text{mV}$ $G = 1.5\ \text{ms}^{-1}$	$\eta_1 = 4.4\ \text{ms}^{-1}$ $\eta_2 = 1.2 \cdot 10^{-2}$ $\eta_3 = 1$

Table 1: Parameters for the simulation on the rectangular slab, taken from [26].

of the parameters of the Roger-McCulloch model – are summarized in Table 1. An electric stimulus is applied by means of the forcing terms $I_{i,e}^s$ of Eq. (3). In particular, we take $I_i^s = 100$ mA in the subdomain $(0, 0.2)$ cm $\times$ $(0, 1)$ cm of Ω; the stimulus is applied from $t = 0$ ms to $t = 1$ ms, and $I_e^s = -I_i^s$ so that the compatibility condition (4) is satisfied. We consider uniform and regular meshes composed of equally sized elements; we denote with h this size. The equations are solved until $T = 175$ ms.

Fig. 3 shows the evolution of the transmembrane potential v. As expected, a potential front is generated in correspondence of the initial stimulus. The duration of the action potential with the chosen parameters of the Roger-McCulloch model is 100 ms; see also Fig. 1 (left). The potential front then "travels" along the longitudinal direction; specifically, we are interested in understanding how the mesh size h and the regularity (continuity) properties of the B-spline basis functions affect its propagation velocity, which we indicate as V_{el}.

The velocity is computed by considering the distance covered by the contourline of a specific value of v – which we set equal to 35 mV – in the time interval $t \in \Delta T = (125, 175)$ ms and dividing this quantity by 50 ms. We assume the "exact" value of velocity to be $V_{ex} = 5.294546 \cdot 10^{-2}$ cm/ms, which is the value computed from an "overkill" solution, obtained by solving the problem with a P3/C0 basis with a very large number of degrees of freedom ($n = 2'365'825$).

Fig. 4 shows the convergence of the velocity V_{el} against the element size h (on the left) and the number of degrees of freedom (on the right) for different B-spline basis functions. First, we remark that the convergence is generally monotone with respect to h and the number of degrees of freedom; in particular, the velocity decreases when the number of degrees of freedom increases. This is consistent with what has been found in [33] for the monodomain equations, i.e. that the Gaussian numerical integration applied to the recovery variables leads to an overestimation of the potential front velocity V_{el}. Moreover, the use of high degree polynomials is indeed beneficial to obtain more accurate approximations of V_{el} when h is smaller than a certain threshold.

Also, the regularity of the basis functions plays a role in the approximation of the potential front velocity. In this regard, we recall that the regularity of the B-spline basis functions depends on the

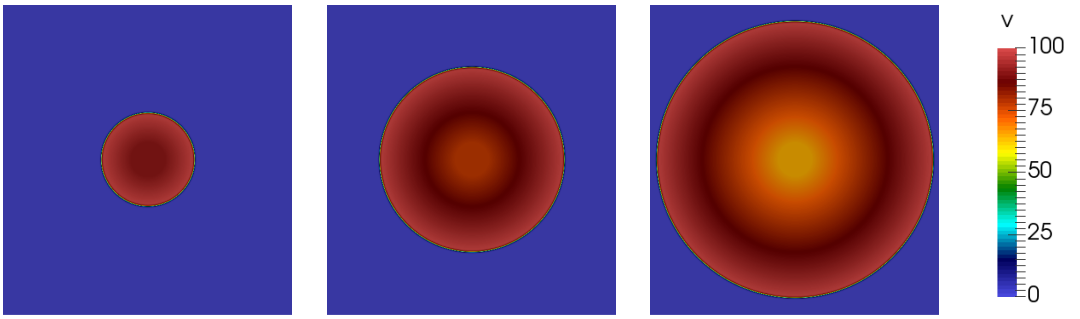

(a) $t = 20$ ms (b) $t = 50$ ms (c) $t = 80$ ms

Figure 5: Solution of the bidomain equations on $\Omega = (-4, 4)\,\text{cm} \times (-4, 4)\,\text{cm}$, obtained by means of P2/C1 basis functions. The initial stimulus $I_i^s = -I_e^s = 100\,\text{mA}$ is imposed from $t = 0\,\text{ms}$ to $t = 1\,\text{ms}$ on a circle of radius $r_c = \sqrt{0.2}\,\text{cm}$ centered at the origin.

p	Continuity	h	n_{dofs}
1	0	0.0156 cm	66'049
2	0	0.0312 cm	66'049
	1	0.0156 cm	66'564
3	0	0.0454 cm	70'255
	2	0.0156 cm	67'081

Table 2: Mesh size h and n_{dofs} for each of the meshes considered in Section 5.2.

multiplicity of the knots (see Section 4.1). Therefore, in order to obtain globally C^0-continuous basis functions when dealing with polynomials of degree $p \geq 1$, the multiplicity of each of the internal knots must match the degree p. Since the number of degrees of freedom n_{dofs} of a univariate basis follows the rule $n_{\text{dofs}} = n_{el} + p$, where n_{el} is the number of internal elements (possibly with zero size), decreasing the regularity of a B-spline basis with high polynomial degree reflects in an increment in n_{dofs}. For this reason, the potential front velocities obtained with P2/C0 and P3/C0 basis functions converge faster to V_{ex} in Fig. 4 (left) with respect to the other more regular basis functions. However, Fig. 4 (right) shows that, when the values of n_{dofs} are comparable, high regularity of the basis also leads to a smaller error in the approximation of V_{ex}. Hence, we have evidence to affirm that the increment of regularity of the basis has positive influence over the approximation of the potential front velocity. Moreover, since the Finite Element Method considers basis functions with C^0-continuity across the mesh elements – which therefore share similar properties with the P1/C0, P2/C0 and P3/C0 basis functions – we infer that IGA performs better than the Finite Element Method in approximating the potential front velocity V_{el}. However, since we did not perform simulations specifically targeted to compare the two methods, our findings should be considered as evidence of the benefits of the high polynomial degree and regularity of B-spline basis functions in this particular application. We remark that similar conclusions about the effectiveness of high continuity of the basis functions were drawn in [38] for the potential front velocity of the solution of the monodomain equations.

5.2. A study of numerical dispersion in a square

We now aim at evaluating the numerical dispersion introduced by the IGA spatial approximation of the bidomain equations. We consider a square slab of tissue $\Omega = (-4, 4)\,\text{cm} \times (-4, 4)\,\text{cm}$ and set the conductivity $\sigma = \sigma_l^{i,e} = \sigma_t^{i,e} = \sigma_n^{i,e} = 1 \times 10^{-3}\,\Omega^{-1}\text{cm}^{-1}$ in Eq. (2) as isotropic and equal for both the intra- and the extracellular spaces, in order to eliminate the anisotropy given by the conductivity tensors $D_{i,e}$. Also in this case, we use the parameters presented in Table 1 for the Roger-McCulloch model. We impose $I_i^s = 100\,\text{mA}$ and $I_e^s = -I_i^s$ in a circle of radius $r_c = \sqrt{0.2}\,\text{cm}$ centered in $\mathbf{x}_c = (0, 0)\,\text{cm}$ from $t = 0\,\text{ms}$ to $t = 1\,\text{ms}$. We exploit the symmetry of the problem and solve it in the first quarter $(0, 4)\,\text{cm} \times (0, 4)\,\text{cm}$. The simulation is run until $T = 80\,\text{ms}$. The solution obtained at different time instances is reported in Fig. 5, where we highlight the circular shape of the potential front. Numerical dispersion errors are revealed when the shape of the computed potential front departs

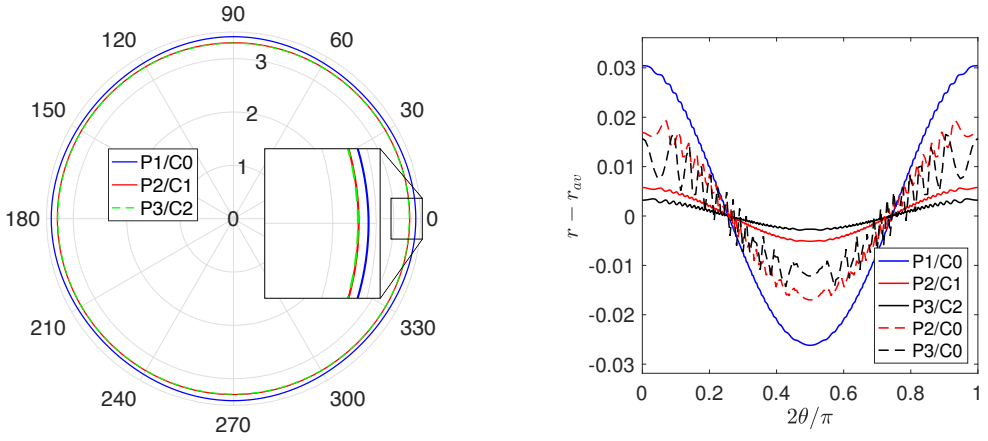

Figure 6: Contourline $r(\theta)$ corresponding to $v = 50\,\text{mV}$ at time $t = 80$ ms for P1/C0, P2/C1 and P3/C2 polynomials (on the left) and difference between $r(\theta)$ and the average distance of the contourline from the origin r_{av} for P1/C0, P2/C1, P3/C2, P2/C0 and P3/C0 polynomials in the first quarter (on the right). We remark that in the right plot the angles have been normalized to 1. The meshes are chosen so that the number of degrees of freedom is approximately constant for all the considered basis functions; the large oscillations in the curves corresponding to high degree polynomials with C^0-continuity are due to the larger sizes characterizing the respective meshes (see Table 2).

from the perfectly circular one. We measure this "distance" to quantify the numerical dispersion error introduced by the spatial discretization.

We use different B-spline basis functions to solve the bidomain equations. As discussed in Section 5.1, basis functions with polynomial degree $p \geq 1$ and continuity smaller than $p-1$ require a considerably larger number of degrees of freedom compared to basis functions with same p but higher continuity, given a fixed mesh size h. Therefore, in order to perform a comparison such that the computational cost is somehow comparable for each of the considered basis functions, we use meshes with approximately the same number of degrees of freedom but different mesh size h. The values of the mesh size and corresponding degrees of freedom are summarized in Table 2.

Fig. 6 provides an analysis of the dispersion error introduced by IGA. On the left, the potential contourlines of $v = 50\,\text{mV}$ at time $t = 80\,\text{ms}$ for P1/C0, P2/C1 and P3/C2 basis functions are compared. Compatibly with the results obtained in Section 5.1, the solution computed with the P1/C0 basis travels faster than the ones corresponding to P2/C1 and P3/C2 basis functions. Moreover, we notice that by increasing the degree of the polynomials and their global continuity the potential front velocity is less and less dependent on the direction of propagation. This is confirmed by Fig. 6 (right), which shows, for different basis functions, the difference between the contourlines $r(\theta)$ – here parametrized with the normalized angle with the x axis in the first quarter – at time $t = 80$ ms and the mean distance (over θ) of the contourline from the point $(0, 0)\,\text{cm}$, which we denote as r_{av}. We remark that, if the potential front were exactly circular, then we would obtain $r(\theta) - r_{av} = 0$ for all θ; this means that the higher $r(\theta) - r_{\text{av}}$, the higher the numerical dispersion error introduced by IGA. We observe that $r(\theta) - r_{\text{av}}$ varies with the angle: in particular, the solutions for all the polynomial basis functions appear to travel faster along the directions of the two axes and achieve minimal velocity in correspondence of $2\theta/\pi = 1/2$, corresponding to the angle $\theta = \pi/4$. This is a consequence of the meshes we adopted, which were composed by squares with edges parallel to the x and y axes, and the type of basis functions we used. Moreover, we notice that $|r(\theta) - r_{\text{av}}|$ decreases both by increasing the degree of the piecewise polynomials while keeping the continuity of the basis constant – this can be observed by comparing P1/C0, P2/C0 and P3/C0 solutions – and by keeping the polynomial degree fixed while increasing the regularity.

In conclusion, our benchmark simulations show that the use of highly regular basis functions with continuity of derivatives across the mesh elements, which is a property characterizing B-splines and NURBS-based IGA from the Finite Element Method, can significantly reduce both the error in the approximation of potential front velocity and the numerical dispersion error.

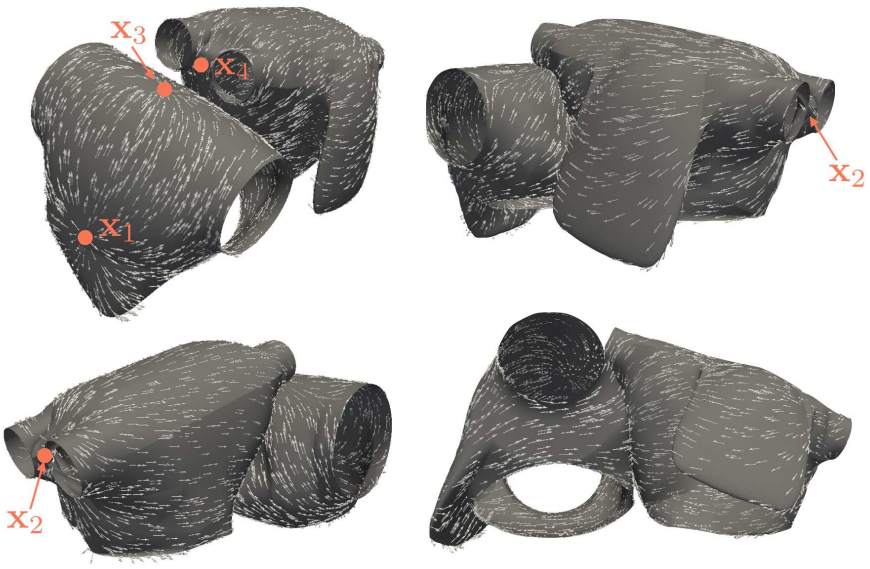

Figure 7: Different views of the atria with fibers direction. The points $\mathbf{x}_1$, $\mathbf{x}_2$, $\mathbf{x}_3$, $\mathbf{x}_4$ are used for fibers construction.

6. Numerical simulation of the electrophysiology of the left and the right atria

We present the results of a numerical simulation performed on surface geometries of both the atria generated by quadratic NURBS functions with global C^1-continuity, except at C^0-lines introduced during the geometric design stage of the surfaces. We use the CRN ionic model for describing the action potential of cardiac cells. The initial condition for the potential is $v_{\text{in}} = -81.2$ mV; we use as initial conditions for the recovery variables the ones reported in [18]. Because of the difficulties arising from the steep upstroke of the action potential, we choose as timestep $\Delta t = 0.01$ ms (lower than the one we used for the benchmark simulations in Section 5) in order to ensure a better approximation of the solution depicted in Fig. 1 (right). We use BDF schemes of order 2 for the time integration.

The right and left atrium surfaces are generated as separated NURBS patches and do not intersect; the interactions among them are based on the hypothesis of the interatrial connections presented in [48]. The underlying assumption, which is supported by physical evidence, is that the septum separating the two upper chambers makes them mutually electrically isolated. The excitation front originating from the sinoatrial node, however, travels from the right to the left atrium through four muscular bundles: the Bachmann's bundle (which is called primary connection because it is typically the first one to be activated), the anterior and the posterior septa, and the coronary sinus musculature. We choose to model the interaction via the external currents: when the potential front reaches the points located on the right atrium representing the contact points of the interatrial connections, a current $I_i^s = 100$ ms is triggered for 1 ms at the corresponding point on the left atrium (as always, by keeping $I_{i,e}^s = -I_i^s$ in order to satisfy the compatibility condition (4)). Since the activation pattern of the left atrium is completely dependent on the propagation on the right one especially in the part of the surface where the excitation is initiated, the elements of the right atrium surrounding the sinoatrial node are characterized by a smaller mesh size h. For this reason, the two geometries are composed by different number of elements: 78'975 for the right atrium and 60'742 for the left atrium.

The bidomain equations require defining the direction of the cardiac fibers to determine the conductivity tensors $D_{i,e}$. In this work, we follow the same strategy that has been adopted in [38, 45, 46] and we assign to the two atria a vector field directed as the gradient of the solution φ of the following Laplace-Beltrami problem [22] defined on the atrial surfaces Ω

$$\begin{aligned} -\Delta_\Omega \varphi &= f \quad \text{in } \Omega, \\ \nabla_\Omega \varphi \cdot \mathbf{n} &= 0 \quad \text{on } \partial\Omega. \end{aligned} \tag{17}$$

We indicate by ∇_Ω is the surface gradient operator, $\mathbf{n}$ is the outward directed unit vector normal to $\partial\Omega$ and $f : \Omega \to \mathbb{R}$ is an arbitrary scalar field such that $\int_\Omega f \, d\mathbf{x} = 0$ (compatibility condition). The forcing term f can be suitable modified to set the orientation of the fibers. The homogeneous

Neumann conditions require to add an additional constraint on φ, e.g. the zero mean value condition $\int_\Omega \varphi \, d\mathbf{x} = 0$.

We then define the local fibers direction $\widehat{\mathbf{a}}_l$ as the gradient unit vector proportional to $\nabla_\Omega \varphi$, namely

$$\widehat{\mathbf{a}}_l := \frac{\nabla_\Omega \varphi}{|\nabla_\Omega \varphi|_2}.$$

Problem (17) is numerically solved by NURBS-based IGA as preprocessing stage of the solver for the bidomain equations. We here outline the steps of the discretization of the equations, which are analogous to the ones presented in Section 4.1. For every $\phi \in \mathcal{V}$ and $\psi \in \mathcal{V}$ (with $\mathcal{V} = H^1(\Omega)$), we introduce the bilinear form

$$a_{\mathrm{LB}}(\phi, \psi) := \int_\Omega \nabla_\Omega \phi \cdot \nabla_\Omega \psi \, d\mathbf{x}.$$

We then consider the weak formulation of the Laplace-Beltrami problem, which reads

(W3) find $\varphi \in \mathcal{V}$, such that

$$a_{\mathrm{LB}}(\varphi, \widetilde{\varphi}) = (f, \widetilde{\varphi}),$$

for all $\widetilde{\varphi} \in \mathcal{V}$.

With the purpose of obtaining the discrete weak formulation, we replace $\mathcal{V}$ with $\mathcal{V}^h \subset \mathcal{V}$, namely the approximation of $\mathcal{V}$ spanned by the NURBS basis functions $\{N_j\}_{j=1}^n$. By replacing φ with $\varphi^h := \sum_{j=1}^n \varphi_j N_j$ and the test function $\widetilde{\varphi}$ with N_j for $j = 1, \ldots, n$, and by introducing the stiffness matrix $(K)_{ij} = a_{\mathrm{LB}}(N_j, N_i)$ and $\mathbf{f} = ((f, N_1), \ldots, (f, N_n))^T$, we find the discrete problem

(W4) find $\boldsymbol{\varphi} = (\varphi_1, \ldots, \varphi_n)^T$ such that

$$K\boldsymbol{\varphi} = \mathbf{f}.$$

Once φ^h is known, the fibers direction is computed as the normalized discrete gradient of the solution, i.e. $\widehat{\mathbf{a}}_l^h := \nabla\varphi^h / |\nabla\varphi^h|_2$. We remark that, being the NURBS basis used for the generation of the atria C^0-continuous at some lines on the surface, the discrete fibers direction is discontinuous at these locations. However, the fibers direction is well defined at the Gauss quadrature points, which are the points at which we actually need the evaluation of the conductivity tensors $D_{i,e}$.

Fig. 7 shows the fibers directions on the two atria computed by solving Eq. (17) with the following forcing term

$$f(\mathbf{x}) = \begin{cases} 1 & \text{if } |\mathbf{x} - \mathbf{x}_1|_2 \leq \delta \text{ or } |\mathbf{x} - \mathbf{x}_2|_2 \leq \delta, \\ -1 & \text{if } |\mathbf{x} - \mathbf{x}_3|_2 \leq \delta \text{ or } |\mathbf{x} - \mathbf{x}_4|_2 \leq \delta, \\ 0 & \text{otherwise }, \end{cases}$$

where $\mathbf{x}_i$ for $i = 1, \ldots, 4$ are points placed on the auricle of the right atrium, between the two external pulmonary veins on the left atrium, on the top part of the right atrium (opposite to the tricuspid valve), and between the two internal pulmonary veins on the left atrium respectively, and δ is the radius of the spheres in which the forcing term is non zero. We remark that the homogeneous Neumann condition in Eq. (17) leads to fibers tangential to the boundary $\partial\Omega$ (which is composed by the borders of the superior and the inferior venae cavae and the tricuspid valve for the right atrium, and by the borders of the pulmonary veins and the mitral valve for the left atrium).

For computing $D_{i,e}$, we use a modified version of Eq. (2) adapted to surfaces that does not require the definition of an orthonormal basis at each $\mathbf{x} \in \Omega$. In particular, we define (similarly to [38])

$$D_{i,e} := \sigma_t^{i,e} I + (\sigma_l^{i,e} - \sigma_t^{i,e}) A_l,$$

where I is the second order identity tensor and A_l is such that $(A_l)_{ii} = (\widehat{\mathbf{a}}_l)_i$ and $(A_l)_{ij} = 0$ if $i \neq j$. The value of the conductivity coefficients $\sigma_l^{i,e}$ and $\sigma_t^{i,e}$, as well as the physical parameters χ and C_m, are summarized in Table 1.

The simulation is initiated by applying the current $I_i^s = 100$ mA and $I_e^s = -I_e^s$ for 1 ms at the sinoatrial node and it is run until $T = 1000$ ms; we consider only one heartbeat.

Fig. 8 shows the action potential and variation of $[\mathrm{Ca}^{2+}]_i$ registered at three points of the domain, i.e. near the sinoatrial node (SA), near the Bachmann's Bundle (BB) on the left atrium, and at the atrioventricular node (AV); in the first two cases, the point is outside the sphere where the external

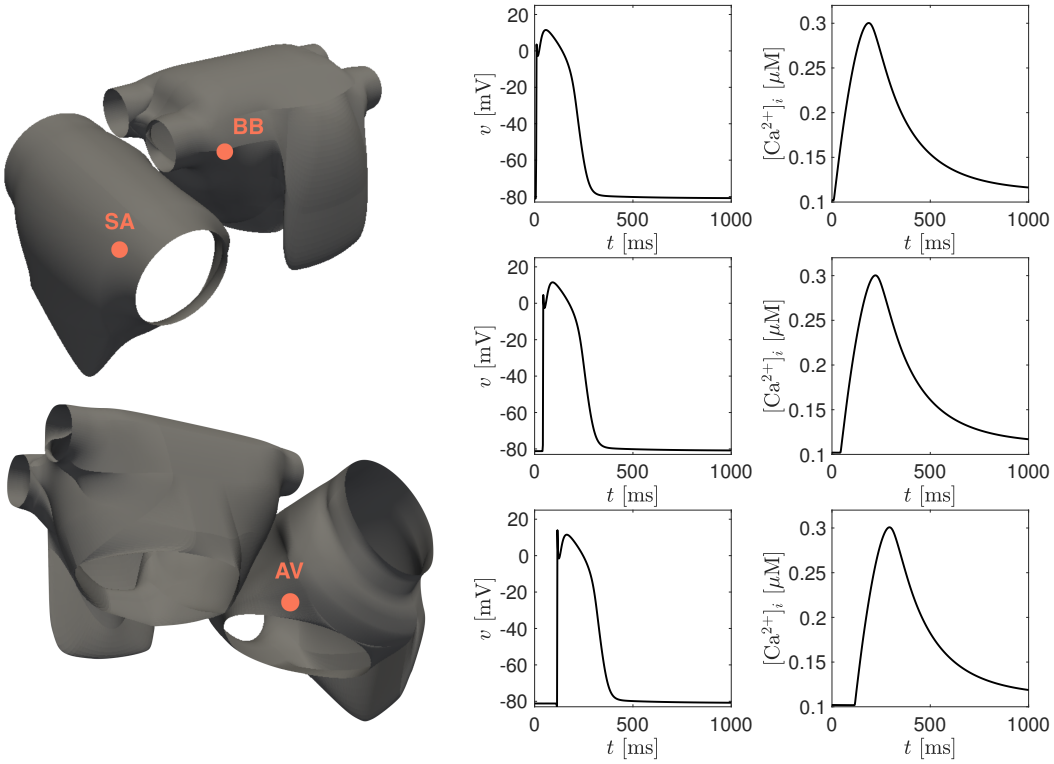

Figure 8: Action potential and evolution of calcium concentration $[Ca^{2+}]_i$ at points near the sinoatrial node (SA, top row), near the Bachmann's Bundle (BB, middle row) and the atrioventricular node (AV, bottom row). The first two points are chosen sufficiently far from the sinoatrial node and the Bachmann's Bundle, so that they are not directly stimulated by the applied initial current.

current is non zero. We remark that the depolarization "wave" reaches the Bachmann's Bundle at $t = 34$ ms, which is a value close to what has been found in [13] (29 ms) with a simulation on atrial surfaces and close to physiological values [14]. The curves of Fig. 8 are similar to the ones depicted in Fig. 1 (right), which refers to the solution of the CRN model for only one cell. While the evolution of calcium $[Ca^{2+}]_i$ registered at the tree locations does not change significantly, the curve of the transmembrane potential varies slightly while traveling throughout the atrial surface. In particular, we notice how, for the points close to the sinoatrial node and the Bachmann's Bundle, the value reached by v during the rapid upstroke of the action potential is lower than expected. This occurs because these points are heavily influenced by the external stimulations applied nearby.

Fig. 9 and Fig. 10 show the evolution of the transmembrane potential v and the intracellular calcium concentration $[Ca^{2+}]_i$.

7. Conclusions

In this work we applied Isogeometric Analysis to the solution of the bidomain equations on surfaces. We performed benchmark numerical simulations that provided meaningful insights on the properties of the transmembrane potential front. In particular, we confirmed that high degree basis functions with high order continuity across the mesh elements manage to accurately approximate the velocity of the potential front. In our simulations, the convergence of the velocity is monotone with respect to the mesh element size h and the number of degrees of freedom n_{dofs}. The same behavior was observed in [33] when the Gaussian integration approach was used for treating the recovery variables in the monodomain equations. Then, we have shown that the use of B-spline basis functions has also an impact on the numerical dispersion error introduced by the spatial discretization. Our results confirm that basis functions featuring high degree piecewise polynomials and with high order continuity across the mesh elements lead to a smaller dispersion error than lower degree basis functions with low continuity, when the number of degrees of freedom – and hence the computational cost – is comparable.

Finally, we presented a realistic numerical simulation on surface atrial geometries generated by means of quadratic NURBS basis functions. In order to simulate the interaction of the two atria,

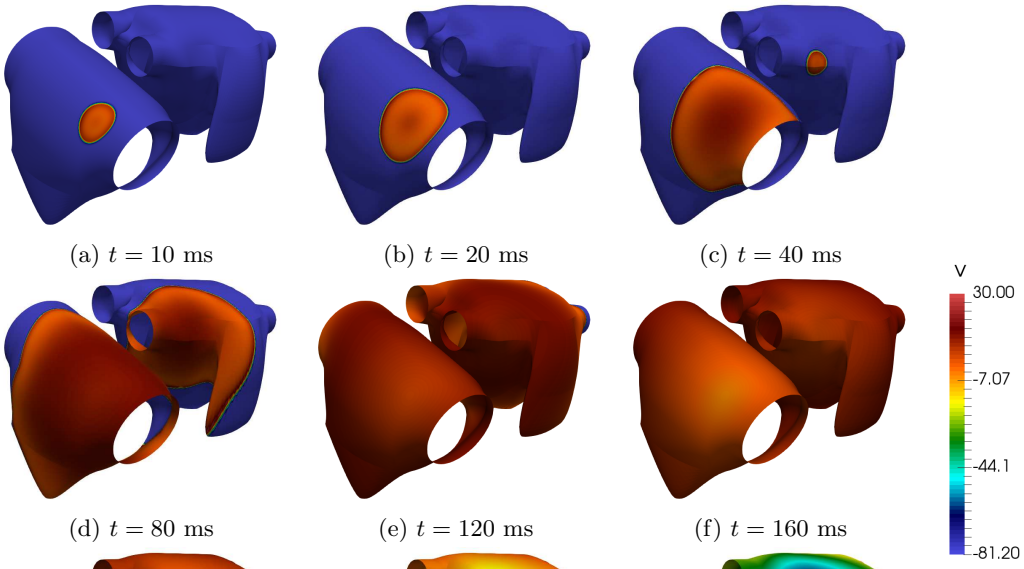

(a) $t = 10$ ms (b) $t = 20$ ms (c) $t = 40$ ms

(d) $t = 80$ ms (e) $t = 120$ ms (f) $t = 160$ ms

(g) $t = 200$ ms (h) $t = 250$ ms (i) $t = 300$ ms

Figure 9: Evolution of transmembrane potential v on both atria.

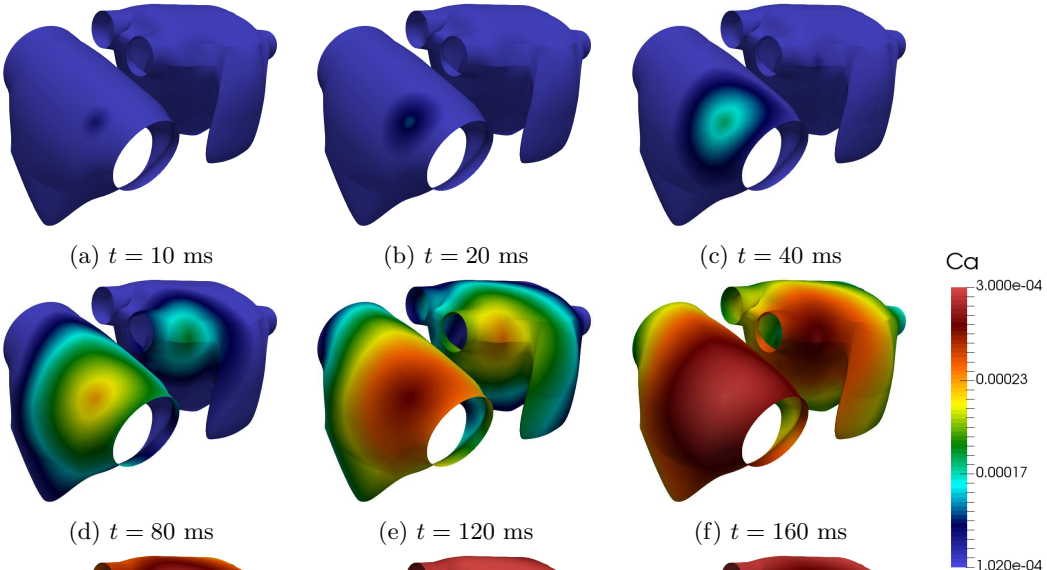

(a) $t = 10$ ms (b) $t = 20$ ms (c) $t = 40$ ms

(d) $t = 80$ ms (e) $t = 120$ ms (f) $t = 160$ ms

(g) $t = 200$ ms (h) $t = 250$ ms (i) $t = 300$ ms

Figure 10: Evolution of intracellular concentration of Ca^{2+} on both atria.

which are represented as separate NURBS patches, we proposed an approach exploiting the hypothesis of interatrial connections. We coupled the bidomain equations with the ionic membrane model proposed by Courtemanche, Ramirez and Nattel, which ensures a realistic approximation of the action potential for atrial cells. Our measurements at different locations of the atria showed that the electric propagation travels with velocity comparable to physiological values and that the "shape" of the action potential is well preserved when traveling on the atrial surface.

Acknowledgments

The authors are grateful to Dr. A. Bartezzaghi for his precious help with isoGlib, the Isogeometric Analysis C++ software library used for the numerical simulations presented in this work.

The second and third authors acknowledge the ERC Advanced Grant *iHEART*, "An Integrated Heart Model for the simulation of the cardiac function", 2017–2022, P.I. A. Quarteroni (ERC–2016–ADG, project ID: 740132).

References

[1] A. Bartezzaghi, L. Dedè, and A. Quarteroni. Isogeometric analysis of high order partial differential equations on surfaces. *Computer Methods in Applied Mechanics and Engineering*, 295:446–469, 2015.

[2] R. Bordas, B. Carpentieri, G. Fotia, F. Maggio, R. Nobes, J. Pitt-Francis, and J. Southern. Simulation of cardiac electrophysiology on next-generation high-performance computers. *Philosophical Transactions of the Royal Society of London A: Mathematical, Physical and Engineering Sciences*, 367(1895):1951–1969, 2009.

[3] Y. Bourgault, Y. Coudiere, and C. Pierre. Existence and uniqueness of the solution for the bidomain model used in cardiac electrophysiology. *Nonlinear Analysis: Real World Applications*, 10(1):458–482, 2009.

[4] A. Bueno-Orovio, E. M. Cherry, and F. H. Fenton. Minimal model for human ventricular action potentials in tissue. *Journal of Theoretical Biology*, 253(3):544–560, 2008.

[5] C. D. Cantwell, S. Yakovlev, R. M. Kirby, N. S. Peters, and S. J. Sherwin. High-order spectral/hp element discretisation for reaction–diffusion problems on surfaces: Application to cardiac electrophysiology. *Journal of Computational Physics*, 257:813–829, 2014.

[6] F. E. Cellier and E. Kofman. *Continuous system simulation*. Springer Science & Business Media, 2006.

[7] L. A. Charawi. *Isogeometric overlapping additive Schwarz preconditioners in computational electrocardioloy*. PhD thesis, Università degli Studi di Milano, 2012.

[8] L. A. Charawi. Isogeometric overlapping additive schwarz solvers for the bidomain system. In T. Dickopf, M. J. Gander, L. Halpern, R. Krause, and L. F. Pavarino, editors, *Domain Decomposition Methods in Science and Engineering XXII*, pages 127–135. Springer, 2016.

[9] P. Colli Franzone, L. Pavarino, and B. Taccardi. Simulating patterns of excitation, repolarization and action potential duration with cardiac bidomain and monodomain models. *Mathematical Biosciences*, 197(1):35–66, 2005.

[10] P. Colli-Franzone, L. F. Pavarino, and S. Scacchi. Mathematical and numerical methods for reaction-diffusion models in electrocardiology. In *Modeling of Physiological flows*, pages 107–141. Springer, 2012.

[11] P. Colli Franzone, L. F. Pavarino, and S. Scacchi. *Mathematical Cardiac Electrophysiology*, volume 13. Modeling, Simulations and Applications, Springer, 2014.

[12] A. Collin, J.-F. Gerbeau, M. Hocini, M. Haïssaguerre, and D. Chapelle. Surface-based electrophysiology modeling and assessment of physiological simulations in atria. In *International Conference on Functional Imaging and Modeling of the Heart*, pages 352–359. Springer, 2013.

[13] A. Collin, J.-F. Gerbeau, M. Hocini, M. Haïssaguerre, and D. Chapelle. Surface-based electrophysiology modeling and assessment of physiological simulations in atria. In *International Conference on Functional Imaging and Modeling of the Heart (2013)*, pages 352–359. Springer, 2013.

[14] F. G. Cosío, A. Martín-Peñato, A. Pastor, A. Nunez, M. A. Montero, C. P. Cantale, and S. Schames. Atrial activation mapping in sinus rhythm in the clinical electrophysiology laboratory. *Journal of Cardiovascular Electrophysiology*, 15(5):524–531, 2004.

[15] J. Cottrell, T. J. R. Hughes, and A. Reali. Studies of refinement and continuity in isogeometric structural analysis. *Computer methods in applied mechanics and engineering*, 196(41):4160–4183, 2007.

[16] J. A. Cottrell, T. J. R. Hughes, and Y. Bazilevs. *Isogeometric Analysis: Toward Integration of CAD and FEA*. John Wiley & Sons, 2009.

[17] J. A. Cottrell, T. J. R. Hughes, and A. Reali. Studies of refinement and continuity in isogeometric structural analysis. *Computer Methods in Applied Mechanics and Engineering*, 196(41):4160–4183, 2007.

[18] M. Courtemanche, R. J. Ramirez, and S. Nattel. Ionic mechanisms underlying human atrial action potential properties: insights from a mathematical model. *American Journal of Physiology-Heart and Circulatory Physiology*, 275(1):H301–H321, 1998.

[19] C. De Boor. On calculating with B-splines. *Journal of Approximation Theory*, 6(1):50–62, 1972.

[20] L. Dedè, C. Jäggli, and A. Quarteroni. Isogeometric numerical dispersion analysis for two-dimensional elastic wave propagation. *Computer Methods in Applied Mechanics and Engineering*, 284:320–348, 2015.

[21] L. Dedè and A. Quarteroni. Isogeometric analysis for second order partial differential equations on surfaces. *Computer Methods in Applied Mechanics and Engineering*, 284:807–834, 2015.

[22] G. Dziuk. Finite elements for the Beltrami operator on arbitrary surfaces. In *Partial differential equations and calculus of variations*, pages 142–155. Springer, 1988.

[23] R. Fitzhugh. Impulses and physiological states in theoretical models of nerve membrane. *Biophysical Journal*, 1(6):445–466, 1961.

[24] D. Forti and L. Dedè. Semi-implicit BDF time discretization of the Navier–Stokes equations with VMS-LES modeling in a High Performance Computing framework. *Computers & Fluids*, 117:168–182, 2015.

[25] P. C. Franzone, L. Pavarino, and S. Scacchi. A comparison of coupled and uncoupled solvers for the cardiac bidomain model. *ESAIM: Mathematical Modelling and Numerical Analysis*, 47(4):1017–1035, 2013.

[26] L. Gerardo-Giorda. Modeling and numerical simulation of action potential patterns in human atrial tissues. From HAL archives-ouvertes: hal-00132706v2, 2008.

[27] A. Gerbi, L. Dedè, and A. Quarteroni. A monolithic algorithm for the simulation of cardiac electromechanics in the human left ventricle. *Mox report 51/2017*, 2017.

[28] D. B. Geselowitz and W. T. Miller III. A bidomain model for anisotropic cardiac muscle. *Annals of Biomedical Engineering*, 11(3-4):191–206, 1983.

[29] H. Gómez, V. M. Calo, Y. Bazilevs, and T. J. R. Hughes. Isogeometric analysis of the Cahn-Hilliard phase-field model. *Computer Methods in Applied Mechanics and Engineering*, 197(49):4333–4352, 2008.

[30] A. L. Hodgkin and A. F. Huxley. A quantitative description of membrane current and its application to conduction and excitation in nerve. *Journal of Physiology*, pages 500–544, 1952.

[31] T. J. R. Hughes, J. A. Cottrell, and Y. Bazilevs. Isogeometric analysis: CAD, finite elements, NURBS, exact geometry and mesh refinement. *Computer Methods in Applied Mechanics and Engineering*, 194(39):4135–4195, 2005.

[32] R. Klabunde. *Cardiovascular Physiology Concepts*. Lippincott Williams & Wilkins, 2011.

[33] S. Krishnamoorthi, M. Sarkar, and W. S. Klug. Numerical quadrature and operator splitting in finite element methods for cardiac electrophysiology. *International Journal for Numerical Methods in Biomedical Engineering*, 29(11):1243–1266, 2013.

[34] I. J. LeGrice, B. Smaill, L. Chai, S. Edgar, J. Gavin, and P. J. Hunter. Laminar structure of the heart: ventricular myocyte arrangement and connective tissue architecture in the dog. *American Journal of Physiology-Heart and Circulatory Physiology*, 269(2):H571–H582, 1995.

[35] C.-H. Luo and Y. Rudy. A model of the ventricular cardiac action potential. Depolarization, repolarization, and their interaction. *Circulation Research*, 68(6):1501–1526, 1991.

[36] C.-H. Luo and Y. Rudy. A dynamic model of the cardiac ventricular action potential. I. Simulations of ionic currents and concentration changes. *Circulation Research*, 74(6):1071–1096, 1994.

[37] D. A. Nordsletten, S. A. Niederer, M. P. Nash, P. J. Hunter, and N. P. Smith. Coupling multiphysics models to cardiac mechanics. *Progress in Biophysics and Molecular Biology*, 104(1):77–88, 2011.

[38] A. S. Patelli, L. Dedè, T. Lassila, A. Bartezzaghi, and A. Quarteroni. Isogeometric approximation of cardiac electrophysiology models on surfaces: an accuracy study with application to the human left atrium. *Computer Methods in Applied Mechanics and Engineering*, 317:248–273, 2017.

[39] M. Pennacchio, G. Savaré, and P. Colli Franzone. Multiscale modeling for the bioelectric activity of the heart. *SIAM Journal on Mathematical Analysis*, 37(4):1333–1370, 2005.

[40] G. Plank, L. Zhou, J. L. Greenstein, S. Cortassa, R. L. Winslow, B. O'Rourke, and N. A. Trayanova. From mitochondrial ion channels to arrhythmias in the heart: computational techniques to bridge the spatio-temporal scales. *Philosophical Transactions of the Royal Society of London A: Mathematical, Physical and Engineering Sciences*, 366(1879):3381–3409, 2008.

[41] A. Quarteroni. *Numerical Models for Differential Problems*. Springer-Verlag, 3rd edition, 2017.

[42] A. Quarteroni, T. Lassila, S. Rossi, and R. Ruiz-Baier. Integrated heart–coupling multiscale and multiphysics models for the simulation of the cardiac function. *Computer Methods in Applied Mechanics and Engineering*, 2016.

[43] A. Quarteroni, R. Sacco, and F. Saleri. *Numerical Mathematics*, volume 37. Springer Science & Business Media, 2010.

[44] J. M. Rogers and A. D. McCulloch. A collocation-Galerkin finite element model of cardiac action potential propagation. *IEEE Transactions on Biomedical Engineering*, 41(8):743–757, 1994.

[45] S. Rossi. *Anisotropic Modeling of Cardiac Mechanical Activation*. PhD thesis, EPFL, 2014.

[46] S. Rossi, T. Lassila, R. Ruiz-Baier, A. Sequeira, and A. Quarteroni. Thermodynamically consistent orthotropic activation model capturing ventricular systolic wall thickening in cardiac electromechanics. *European Journal of Mechanics - A/Solids*, 48:129–142, 2014.

[47] R. Ruiz-Baier, A. Gizzi, S. Rossi, C. Cherubini, A. Laadhari, S. Filippi, and A. Quarteroni. Mathematical modelling of active contraction in isolated cardiomyocytes. *Mathematical Medicine and Biology*, 31(3):259–283, 2013.

[48] S.-I. Sakamoto, T. Nitta, Y. Ishii, Y. Miyagi, H. Ohmori, and K. Shimizu. Interatrial electrical connections: the precise location and preferential conduction. *Journal of Cardiovascular Electrophysiology*, 16(10):1077–1086, 2005.

[49] E. Schenone, A. Collin, and J.-F. Gerbeau. Numerical simulation of electrocardiograms for full cardiac cycles in healthy and pathological conditions. *International Journal for Numerical Methods in Biomedical Engineering*, 2015.

[50] J. Sundnes, G. T. Lines, X. Cai, B. F. Nielsen, K.-A. Mardal, and A. Tveito. *Computing the Electrical Activity in the Heart*, volume 1. Monographs in Computational Science and Engineering, Springer, 2007.

[51] A. Tagliabue, L. Dedè, and A. Quarteroni. Isogeometric analysis and error estimates for high order partial differential equations in fluid dynamics. *Computers & Fluids*, 102:277–303, 2014.

[52] N. A. Trayanova. Whole-heart modeling: applications to cardiac electrophysiology and electromechanics. *Circulation research*, 108(1):113–128, 2011.

[53] L. Tung. *A Bi-domain Model for Describing Ischemic Myocardial D-C Potentials*. PhD thesis, Massachussets Institute of Technology, 1978.

[54] C. Vergara, S. Palamara, D. Catanzariti, F. Nobile, E. Faggiano, C. Pangrazzi, M. Centonze, M. Maines, A. Quarteroni, and G. Vergara. Patient-specific generation of the Purkinjehe network driven by clinical measurements of a normal propagation. *Medical & Biological Engineering & Computing*, 52(10):813–826, 2014.

[55] E. Vigmond, F. Vadakkumpadan, V. Gurev, H. Arevalo, M. Deo, G. Plank, and N. Trayanova. Towards predictive modelling of the electrophysiology of the heart. *Experimental Physiology*, 94(5):563–577, 2009.